Open-access testbench data for NVH benchmarking of e-machines under electromagnetic excitations

Emile Devillers[1,2], Karine Degrendele[1], Michel Hecquet[2], Jean-Philippe Lecointe[3], Jean Le Besnerais[1], Guillaume Cousin[4]
[1]EOMYS ENGINEERING, Lille Hellemmes, France
[2]L2EP, Villeneuve d'Asq, France
[3]LSEE, Béthune, France
[4]OROS, Meylan, France

Abstract

This paper presents an experimental setup dedicated to the analysis of noise and vibration due to Maxwell magnetic forces in electrical machines, a significant NVH source in hybrid and electric vehicles traction motors. Both electromagnetic excitations and structural response of the electrical machine are simplified to provide the first public benchmark of e-NVH phenomenon (electromagnetic Noise, Vibration, Harshness).

The paper first describes how the testbench is designed and tested in order to reduce as much as possible modelling and experimental uncertainties. A Permanent Magnet Synchronous Machine topology used in EV/HEV applications is used to illustrate tooth modulation effect and interaction between radial and tangential force-induced vibrations, and designed to generate the resonance of several stator structural modes with simplified electromagnetic loading (open-circuit case). A larger air gap allows the insertion of a fine search-coil network to measure time and space distribution of the air-gap flux density and resulting Maxwell stress harmonics. Accelerometers are placed on stator tooth tips to capture tooth bending motion, as well as on the outer yoke of the stator. Besides vibration measurements, sound pressure and sound power level measurements are carried.

Then, some of the key measurement results are presented including Experimental Modal Analysis, Operational Deflection Shapes, and Order Tracking Analysis, spectrograms and spatiograms, Sound Pressure Level and Sound Power Level measurements. The origin of the different NVH harmonics are analyzed and their physical origin is detailed.

All the benchmark data is available in open access and can be used to compare different multiphysic simulation strategies of e-NVH in terms of accuracy and computing time, such as analytic, semi-analytic, numerical and hybrid methods using during electromagnetic, structural mechanics and acoustic calculations. The benchmark will be used in further work to study the most common noise mitigation strategies used in EV/HEV electric motors such as skewing, notching, pole and slot shaping, and harmonic current injection.

Introduction

Magnetic forces in electrical machines are a significant source of NVH, which can be responsible of high tonal noise. Multi-physics modeling including electric, electromagnetic, structural and acoustic calculations is performed to predict noise levels at a design stage.

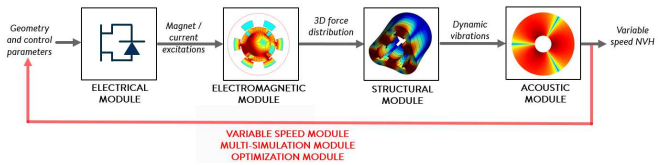

Figure 1. Multi-physics modeling for noise and vibration assertion in e-machines [1]

Different simulation strategies of e-NVH are available such as analytic, semi-analytic, numerical and hybrid methods [2]. However, the literature does not address some key aspects of the multi-physics modeling leading to uncertainties on the noise prediction. It includes the interaction between radial and tangential forces, the spatial sampling effect of tooth on air gap magnetic field and the impact of stator yoke structural resonances.

This paper first describes the key design criteria of a testbench which aims at comparing and validating the above simulation methods. It then demonstrates key measurements, post processes and analyses to capture the root cause of e-NVH harmonics. Finally, it emphasizes the importance of sharing comprehensive data with the research community to tackle non-reproducible and non-sustainable articles due to a lack of input data.

Testbench design

Key design criteria

The testbench is intentionally designed to be noisy while keeping its concept as simple as possible. A summary of its key design criteria is provided below:

- It should magnetically excite the ovalization mode $\boldsymbol{m = 2}$ of the external stator structure in the audible frequency range so that resonance is clearly identified and isolated.
- Number of teeth should be reduced to allow tangential effect and tooth modulation to be investigated.
- Instrumentation access and location should be integrated at early design stage. A larger air gap allows on one hand the insertion of a fine search-coil network to measure time and space distribution of the air-gap flux density and resulting Maxwell stress harmonics, on the other hand the insertion of an air-gap radial flux sensor. A large slot opening width allows the insertion of a triax accelerometer on teeth.
- Its magnetic force harmonic content should be finite and sparse to unambiguously identify each electromagnetic excitation. The electromagnetic loading is therefore simplified with an open-circuit case. A Surface Permanent Magnet Synchronous Motor

(SPMSM), which is a synchronous motor whose field excitation is provided by surface permanent magnets on the rotor, is selected. Its electromagnetic forces are only due to the interaction of rotor MagnetoMotive Force (MMF) harmonics with stator permeance ones.
Rotor slotting, saturation and PWM harmonics are not present in the stress harmonic content since a smooth rotor with surface magnets is selected, the stator yoke is designed not to saturate with rotor MMF and a driving machine is used to spin the rotor (no load).

- Large resonances occur at two conditions: the electromagnetic excitation frequency must match a natural frequency, and the electromagnetic excitation wavenumber must match the corresponding modal shape of the stator (or rotor). Generally, in EV/HEV electric traction applications, the lowest natural frequency is the ovalization mode.

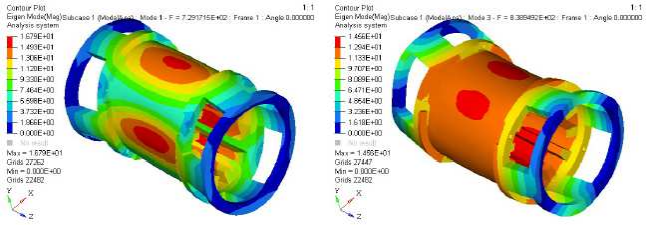

(a) Ovalization mode at (f_{20} = 729 Hz, 2, 0) (b) Bending mode at (f_{10} = 838 Hz, 1, 0)

Figure 2. Modal shapes of benchmark machine with both end rings locally clamped (around bolts)

Number of poles and teeth of the benchmark machine in open-circuit should comply with the following formula:

$$\boldsymbol{r_{min} = \mathrm{gcd}(Z_s, 2p) = 2} \quad (1)$$

to ensure the presence of stress harmonics with wavenumber $\boldsymbol{r = 2}$ that can excite stator ovalization mode.

Based on all those criteria and to be representative of commonly-used industrial topologies (e.g. in the automotive sector), the chosen topology is a SPMSM $\boldsymbol{12s10p}$, i.e. with 12 stator slots ($\boldsymbol{Z_s = 12}$) and 10 poles ($\boldsymbol{2p = 10}$).

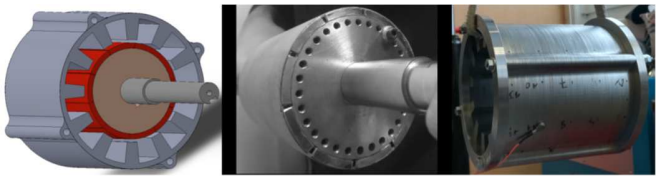

Figure 3. Surface Permanent Magnet rotor and stator lamination stack (Left: Stator in Grey, rotor in red; Middle: rotor; Right: Stator lamination stack)

The driving machine is a DC machine for the easy variable speed command which only requires a programmable DC voltage supply. The DC machine can reach 3300 RPM without load. The stator lamination stack is pressurized by four bolts through two lateral rings to the vertical endshields to a tightening torque of 7N.m. The lateral rings have holes to enable the passing of instrumentation wiring, e.g. for accelerometers, search coils, etc. The SPMSM 12s10p and the driving machine are screwed on two independent T-slot tables, which are screwed on a common frame using silent blocks to reduce the vibration transmission through the base frame. The T-slot tables are orthogonal to set the alignment of both machines in the two directions of the base frame plane. The third direction (vertical direction) can be also adjusted since the driving machine is mounted on a vertical rail. Both machines can be coupled with a mechanical coupling (see Figure 4) or a magnetic coupling (see Figure 13) to limit the transmission of torque ripple and axial force ripple, and also limit the effect of shaft eccentricity. However, the magnetic coupling decreases the maximum transmitted torque and creates a constant axial force between both shaft which solicit the silent blocks and bend the driving machine. It also stresses the bearings in the axial direction and requires the use of conical bearings. Therefore, the measurements presented in the following are performed with the mechanical coupling, even if rotor vibrations of the driving machine may be directly transmitted to the surface PM rotor.

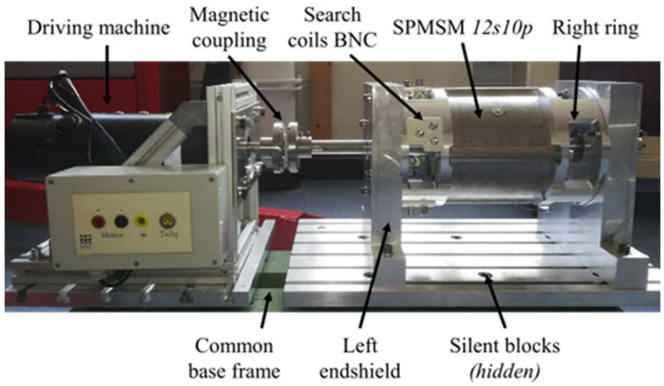

Figure 4. Testbench prototype

Main stress harmonic content and their origin

Time and space harmonic content of radial and circumferential airgap stress distribution of the testbench machine under open-circuit condition are calculated using the analytical resolution of Maxwell equations and the Maxwell Stress Tensor in the middle of the airgap [3]. These stress harmonics are applied at the interface between the airgap and the external structure which result in vibration and noise generation. Each magnetic stress harmonic originates from several combinations of flux density harmonics, which come from several combinations of stator permeance harmonics (due to slotting effect at stator side) and rotor MMF harmonics (due to the distribution of permanent magnets at rotor side). The main combinations of flux density harmonics and their main respective combinations of permeance and MMF harmonics are represented in Table 1.

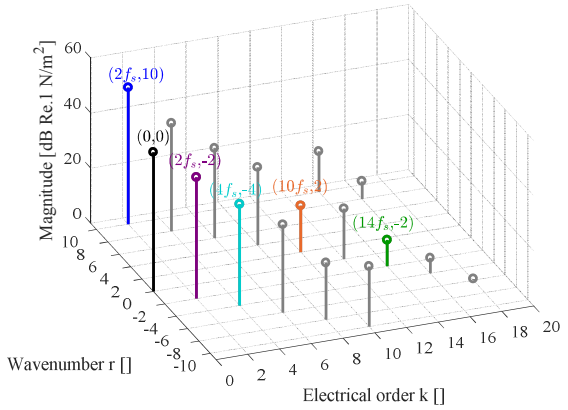

Figure 5. Main air gap stress harmonic of the testbench machine

Table 1. Main air gap stress harmonic of the testbench machine and their main origins

Stress harmonic $\sigma_i(kf_s, r)$	1st flux density harmonic $B_{i1}(kf_s, r)$		2nd flux density harmonic $B_{i2}(kf_s, r)$	
	Permeance $\Lambda_{i1}(kf_s, r)$	MMF $F_{i1}(kf_s, r)$	Permeance $\Lambda_{i2}(kf_s, r)$	MMF $F_{i2}(kf_s, r)$
$\sigma_1(2f_s, 10)$	$B_{11}(f_s, 5)$		$B_{12}(f_s, 5)$	
	$\Lambda_{11}(0,0)$	$F_{11}(f_s, 5)$	$\Lambda_{12}(0,0)$	$F_{12}(f_s, 5)$
$\sigma_2(2f_s, -2)$	$B_{21}(f_s, 5)$		$B_{22}(f_s, -7)$	
	$\Lambda_{21}(0,0)$	$F_{21}(f_s, 5)$	$\Lambda_{22}(0, -12)$	$F_{22}(f_s, 5)$
$\sigma_3(4f_s, -4)$	$B_{31}(3f_s, 15)$		$B_{32}(f_s, -19)$	
	$\Lambda_{31}(0,0)$	$F_{31}(3f_s, 15)$	$\Lambda_{32}(0, -24)$	$F_{32}(f_s, 5)$
$\sigma_4(10f_s, 2)$	$B_{41}(11f_s, 55)$		$B_{42}(-f_s, -53)$	
	$\Lambda_{41}(0,0)$	$F_{41}(11f_s, 55)$	$\Lambda_{42}(0, -48)$	$F_{42}(-f_s, -5)$

Experimental tests, results and analyses

Several experimental measurements are performed to identify the electromagnetically-induced vibration waves responsible for acoustic noise. The origin of the different NVH harmonics are analyzed based on different post-processings (spectrogram, ordogram, ODS, spatiogram) which enable to linked to the harmonic content of stator vibration to that of the magnetic stress distribution. Measurements and post-processings are performed using OROS OR35 and OR36 modules.

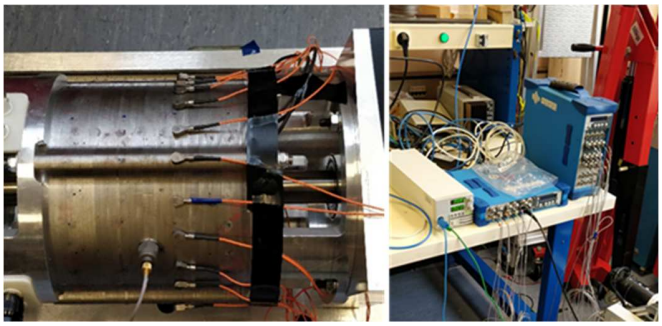

Figure 6. Benchmark prototype instrumented with 20 accelerometers, experimental platform (right)

Surface PMs magnetization

The real pattern of the rotor magnetization can be measured in the air using a Hall effect probe, as illustrated in Figure 7. The measured magnetization is compared with ideal magnetization (parallel or diametrical magnetization). The main components are the odd multiple of the number of pole pairs p but other small harmonics also exist due to uneven magnetization and rotor eccentricity.

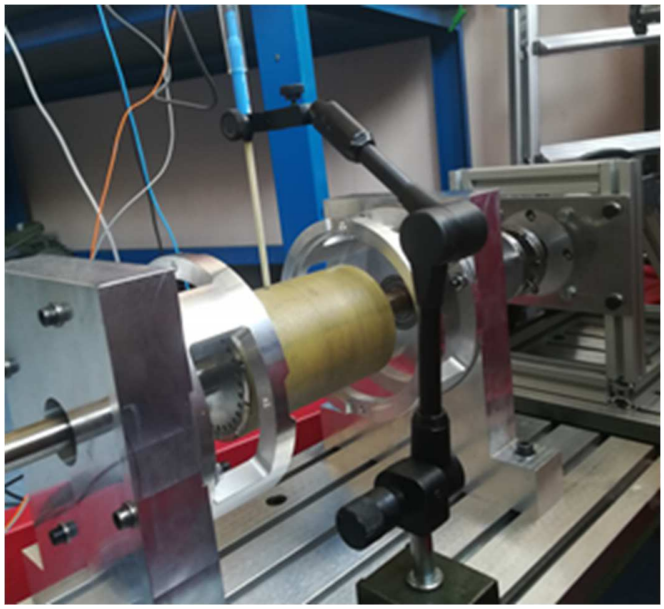

Figure 7. Rotor magnetization measurement with a Hall effect probe

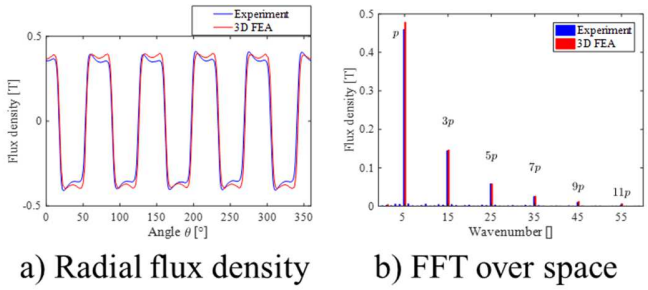

Figure 8. Comparison between measured and ideal rotor magnetization patterns

Air gap flux density

A search coil wounded around a stator teeth captures the induced voltage by time-varying magnetic flux. This signal can be integrated in a standard NVH acquisition system (similarly as acceleration is integrated to obtain the velocity) to get a picture of the average radial flux density over a given stator tooth. The radial magnetic force applied to stator teeth can be approximated as the square of the average radial magnetic flux. A Frequency Response Function can therefore be estimated by making the ratio between the radial displacement and the radial tooth force.

EMA

As the electromagnetic forces can easily excite the radial structural modes of the stator structure, an EMA using a roving shock hammer and accelerometers is performed on the stator yoke to determine modal deflection shapes, natural frequencies and modal damping of the structure.

Frequency Response Functions (FRF) is obtained by post-processing within the acquisition software. It represents the structure mechanical response subject to hammer excitation.

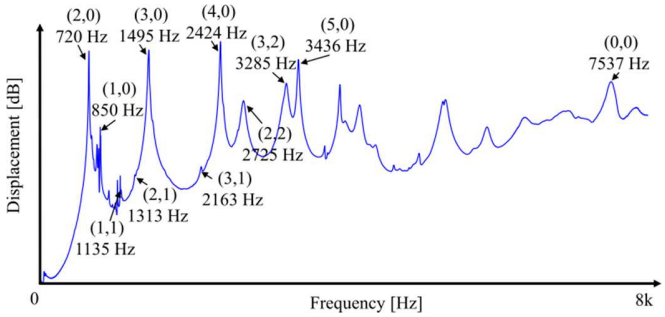

Figure 9. Experimental radial FRF obtained from EMA on testbench machine

From Figure 9, natural frequencies of radial modes ($m = \{0;\ 1;\ 2;\ 3;\ 4\},\ n = 0$) appear at respectively at $f_{0,0} = 7537$ Hz, $f_{1,0} = 850$ Hz, $f_{2,0} = 720$ Hz, $f_{3,0} = 1495$ Hz, $f_{4,0} = 2424$ Hz. Other peaks exist in the radial FRF due to the excitation of radial modes with higher circumferential orders (e.g. $m = 5$), and also the excitation of longitudinal modes such as ($m = 2,\ n = \{1;2\}$) and ($m = 3,\ n = \{1;2\}$). The radial FRF enables to measure the real damping ratios $\xi_{m,n}$ associated to each structural mode ($f_{m,n},\ m,\ n$).

Beyond all the structural modes of the structure highlighted above, some of them are not excited by operational magnetic forces and some of them are shifted under operational conditions (due to temperature, boundary conditions…). Damping is generally significantly impacted by temperature so the usage of the damping value extracted from EMA at ambient (not operational) temperature is limited.

Spectrogram

A spectrogram visualizes a frequency spectrum in function of time or rotating speed (based on a tachometer signal). Rotating speed of the benchmark rotor is controlled by the driving machine, measured by a tachometer and set to be increased linearly between 0 and 1200RPM over 40s. Acceleration of the outer yoke in radial direction is recorded during the linear ramp-up. The time signal is split into 500 horizontal slices with an overlap of 75%. The figure below overlays the frequency spectrums associated to each slice.

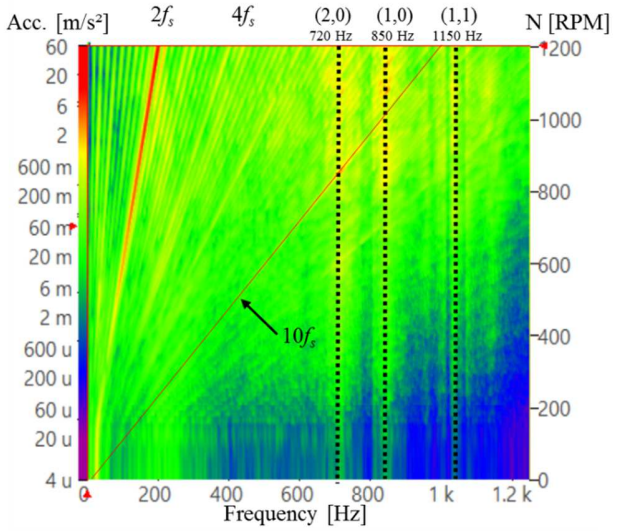

Figure 10. Radial acceleration spectrogram

The main forced excitation which appears as straight lines crossing the origin of the graph, occurs at $2f_s$. As mentioned in Table 1, it is mainly due to the superposition of the fundamental stress $(2f_s, 10)$ and the first slotting stress harmonic $(2f_s, -2)$.

Three distinct structural mode natural frequencies of the stator yoke appear as vertical bands on the spectrogram: ovalization mode at 720 Hz, bending mode at 850 Hz and (1,1) mode at 1150 Hz.

A resonance between the higher slotting harmonics $(10f_s, 2)$ and the ovalization mode is clearly noticeable at 720 Hz and 850 RPM.

Order Tracking

The equivalent of a spectrogram can be drawn as an ordogram, where the x-axis directly represents the mechanical orders k instead of the frequency.

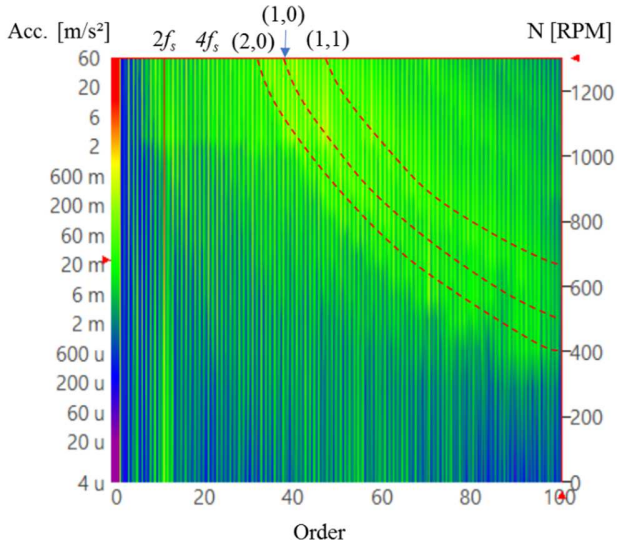

Figure 11. Radial acceleration ordogram

The exact expression of the main electromagnetic force frequency can then be easily identified as $f = 10f_R = 2f_s$ (using f: frequency of the excitation force, f_R: mechanical frequency, f_s: electrical frequency).

An Order Tracking at the order 50 is performed to investigate further the resonances of the higher slotting harmonics $(10f_s, 2)$. It consists in extracting the signal magnitude at $50f_R = 10f_s$ along the RPM axis and gives an image of the dynamic mechanical transfer function of the stator, and both natural frequencies and damping factor can be estimated using respectively the equations below:

Natural frequency: $\boldsymbol{f_{nat,k} = \frac{kN_0}{60}}$ (2)

Damping $\boldsymbol{\xi = \frac{\Delta N}{2N_0}}$ (3)

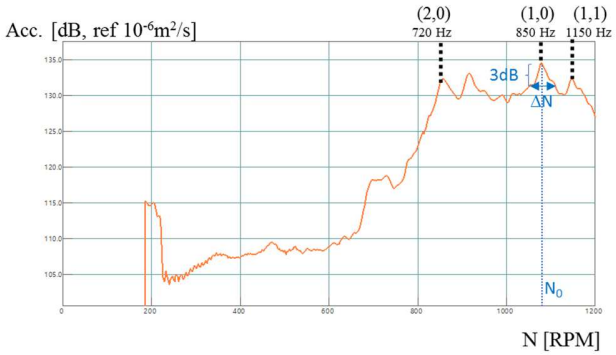

Figure 12. Order Tracking of order 50 from acceleration ordogram

ODS

The Operational Deflection Shape (ODS) enables to visualize the stator stack deflection shape at a certain frequency and a certain speed, the structure being excited by its internal operational excitation forces. It provides physical insight on the interaction between stress harmonics and the stator structure of the electrical machine. The experimental set up is illustrated in Figure 13.

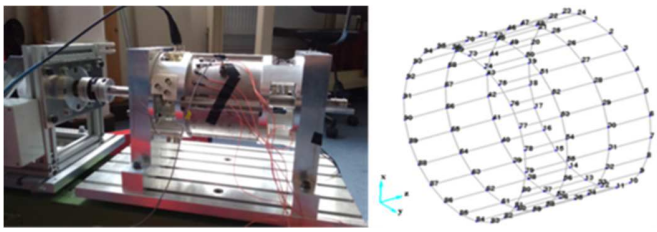

Figure 13. ODS measurement set-up using 6 roving accelerometers (left) on a 96 nodes geometry (right)

Vibrations are measured using 6 roving accelerometers and 1 reference accelerometer located on the outer yoke of the stator. The 6 roving accelerometers are moved 16 times to map the 96 nodes of the whole geometry. With this setup, the ODS can capture radial modes with circumferential wavenumbers up to 12 and axial wavenumbers up to 2 according to Shannon theorem (24 nodes per circumference plane).

The forced response of the SPMSM stator is investigated at 550 RPM where no resonance is noticed on the acceleration spectrogram.

Deflections due to the forced stress harmonics $(2f_s, -2)$, $(4f_s, -4)$, $(10f_s, -2)$ are illustrated in Figure 14. There are rotating waves as the exciting frequencies are far from the natural frequency of their corresponding structural mode. Besides the rotation direction is well captured as $(2f_s, -2)$ and $(4f_s, -4)$ rotates in the opposite direction compared to $(10f_s, 2)$.

However, the deflection due to the fundamental stress $(2f_s, 10)$ is not visually noticeable at $2f_s$. This may be explained by the stiffness of the stator structure which filters the main stress harmonic of wavenumber $r = 10$, or by the fact that this stress harmonic of wavenumber $r = 10$ is modulated by the stator teeth due to spatial aliasing.

The ODS highlights a dynamic eccentricity which creates harmonics of frequency $f = 2f_s + f_R$ and which excites stator bending mode around 850 Hz.

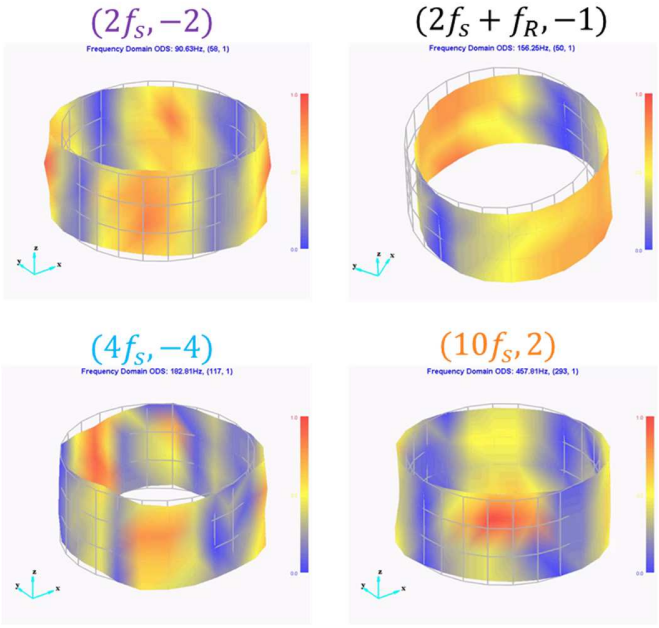

Figure 14. Rotating deflections of the stator yoke at 850RPM due to expected forced excitations at $(2f_s, -2)$, $(4f_s, -4)$, $(10f_s, -2)$ and unexpected UMP excitation at $(2f_s + f_R, -1)$

As presented, an ODS is based on a visual check which may be misleading as animation are usually in linear scale.

Circumferential effects

The influence of circumferential effects, i.e. the influence of circumferential flux density on radial stress and the influence of circumferential stress on radial vibrations cannot be directly measured in the SPMSM. Circumferential effects are investigated based on an experiment with three stator teeth having a tri-axes accelerometer on their side (cf. Figure 15) to measure radial and circumferential accelerations at tooth tip. Besides, three mono-axis accelerometers are put on the stator yoke external surface in front of the stator teeth with a tri-axes accelerometer. Radial and circumferential accelerations at tooth tip are compared with the radial acceleration of the yoke in front of the tooth in Figure 15, at 850 RPM. The magnitude of yoke radial acceleration at $2f_s$ is 7 m/s² while magnitudes of tooth radial and circumferential accelerations are respectively 5.7 m/s² and 5.2 m/s².

Therefore, the magnitude difference between stator yoke and tooth tip radial acceleration is around 19% (i.e. 0.9 dB on acceleration level and 1.8 dB on SWL level), and can be explained by the circumferential acceleration at tooth tip which also contributes to yoke radial acceleration due to tooth bending motion. Besides, the ratio is naturally not the same for each acceleration harmonics as it depends on their phase shift angle, which yields constructive or destructive interferences.

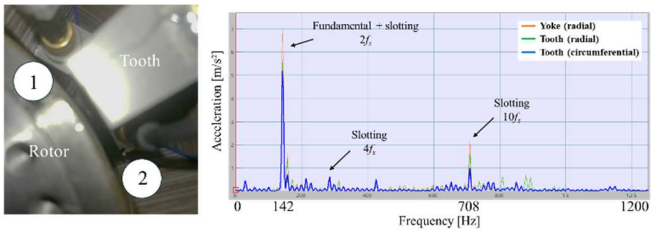

Figure 15. Triax accelerometers located on tooth side (left, acceleration FFT at 850RPM (right)

Spatiogram

A "spatiogram" is based on the spectrogram visualization of the vibration waves filtered by wavenumbers [4]. It allows to quickly and efficiently discriminate the wavenumbers r of the electromagnetic excitation waves and quantify their respective contributions.

The intent is to study the contribution of each wavenumber up to a maximum wavenumber $r = 10$. It dictates the testbench to be equipped with 20 accelerometers evenly distributed along the circumference according to Shannon theorem (see Figure 6). For each wavenumber r, a spatial average is calculated from the 20 synchronized time signals (see (1)), then a FFT is applied to the average signal.

$$A^r(t) = \frac{1}{N_{acc}} \sum_{i=1}^{N_{acc}} e^{j\alpha_i r} a_i(t) \quad (1)$$

Where: N_{acc} : Number of accelerometers
α_i : Angle of accelerometer i [rad]
r : Circumferential wavenumber
$a_i(t)$: Radial acceleration of accelerometer i at t [m/s2]

Figure 16 and Figure 17 show the resulting spatiograms for $r = -2$ and $r = 10$.

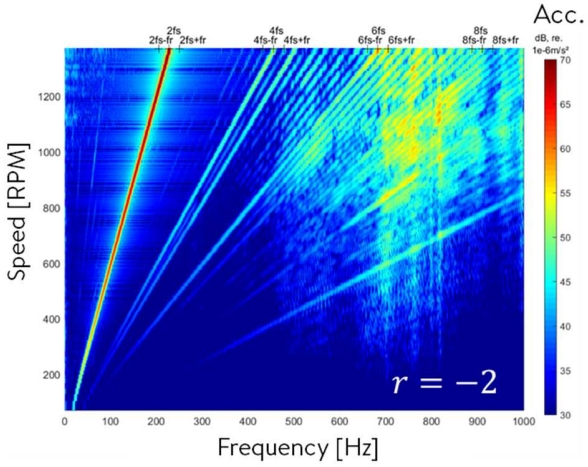

Figure 16. Spatiogram of $r = -2$

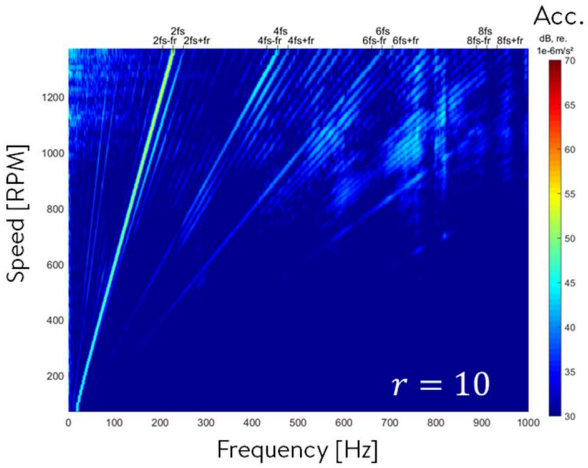

Figure 17. Spatiogram of $r = 10$

The biggest contributor to the excitation occurring at $2f_s$ can obviously be identified comparing both spectrograms. Indeed, significantly higher acceleration levels are noticed on the straight line at $2f_s$ for $r = -2$, which means the excitation actually mostly comes from the first slotting stress harmonic ($r = -2$). This method is quicker and more robust than an ODS.

Acoustic

SPMSM 12s10p Sound Power Level will be characterized inside a semi-anechoic chamber. The test bench will be centered in the chamber and an acoustic enclosure will be erected around the driving machine to isolate its noise. Sound Pressure Level measurements are scheduled using microphones located around the test bench. Results will be publicly shared [5] and be used to validate acoustic models.

Open source data

The testbench can be referred as the first benchmark of the phenomenon of electromagnetically-excited noise and vibrations.

The intent is to provide to the scientific community a datapaper gathering exhaustively the benchmark data to facilitate data management, ensure accessible, interoperable and reusable data, avoid any concern of replicability making the data more valued.

Data includes inputs (geometry, sensor database,…), results, etc., which are produced in a normalized format.

The webpage dedicated to the benchmark project can be found on EOMYS website [5].

Results can then be reused by the scientific community for future research to compare different multiphysic simulation strategies of e-NVH in terms of accuracy and computing time, such as analytic, semi-analytic, numerical and hybrid methods using during electromagnetic, structural mechanics and acoustic calculations.

The datapaper could as well serve as a database for any member of the community to add their respective experimental or simulation data.

References

1. MANATEE, “Magnetic Acoustic Noise Analysis Tool for Electrical Engineering,” 2018. [Online]. Available: www.manatee-software.com
2. Devillers, E., Hecquet, M., Cimetière, X., Lecointe, J-P. et al., “Experimental Benchmark for Magnetic Noise and Vibrations Analysis in Electrical Machines,” *ICEM 2018 Proceedings.*
3. Devillers, E., “Electromagnetic subdomain modeling technique for the fast prediction of radial and circumferential stress harmonics in electrical machines,” *PhD 2018.*
4. Souron, Q., Le Besnesrais, J., Hecquet, M., “Analysis of electromagnetically-induced vibrations of electrical machines based on spatiogram technique,”, *ISEF 2015*
5. Eomys Engineering, “e-NVH benchmark”, 2018. [Online]. Available: https://www.eomys.com/recherche/article/e-nvhbenchmark

Contact Information

Emile Devillers
121, rue de Chanzy - Hellemmes - CS 10128 59030 Lille Cedex - FRANCE
emile.devillers@eomys.com

Definitions/Abbreviations

EMA	Experimental Modal Analysis
EV	Electric Vehicle
f_R	Mechanical frequency
FRF	Frequency Response Function
f_S	Electrical frequency
GCD	Great Common Divisor
HEV	Hybrid Electric Vehicle
k	Mechanical order
MMF	MagnetoMotive Force
NVH	Noise, Vibration, Harshness
ODS	Operational Deflection Shape
OT	Order Tracking
p	Number of pair of poles
PWM	Pulse Width Modulation
r	Wavenumber
SPMSM	Surface Permanent Magnet Synchronous Motor
Zs	Number of stator teeth